Available online at www.sciencedirect.com
SCIENCE DIRECT®
Journal of Nuclear Materials 323 (2003) 81–92
journal of nuclear materials
www.elsevier.com/locate/jnucmat

Host phases for actinides in simulated metallic waste forms

Dawn E. Janney *

Argonne National Laboratory – West, P.O. Box 2528, Idaho Falls, ID 83403-2528, USA

Received 27 January 2003; accepted 18 August 2003

Abstract

Argonne National Laboratory has developed an electrometallurgical process for conditioning spent sodium-bonded metallic reactor fuel prior to disposal. A waste stream from this process consists primarily of stainless steel cladding hulls containing undissolved metal fission products and a low concentration of actinide elements. This waste will be immobilized in a metallic waste form whose baseline composition is stainless steel alloyed with 15 wt% Zr (SS–15Zr). This paper presents transmission electron microscope, energy-dispersive X-ray spectroscopy, and electron diffraction observations of SS–15Zr alloys containing 2–11 wt% U, Np, or Pu. The major U- and Pu-bearing materials are Cr–Fe–Ni–Zr intermetallics with structures similar to that of the C15 polymorph of Fe_2Zr, significant variability in chemical compositions, and 0–20 at.% actinides. A U-bearing material similar to the C36 polymorph of Fe_2Zr had more restricted chemical variability and 0–5 at.% U. Uranium concentrations between 0 and 5 at.% were observed in materials with the $Fe_{23}Zr_6$ structure.

1. Background

Argonne National Laboratory has developed an electrometallurgical process for conditioning spent sodium-bonded metallic reactor fuel prior to disposal at the Yucca Mountain site in southern Nevada [1–3]. The process uses electrorefining to separate fission products and actinides. During electrorefining, chopped spent fuel is partially dissolved in a LiCl–KCl eutectic salt. Actinide elements are electrotransported through the salt and deposited at cathodes; undissolved material (primarily fuel cladding hulls) remains at the anode. The undissolved material includes zirconium from alloy fuels, metal fission products such as Tc, Ru, Rh, Pd, and Ag, and a low concentration of actinide elements (U, Np, and Pu). This material will be immobilized in a metallic waste form whose baseline composition is stainless steel alloyed with 15 wt% Zr (SS–15Zr).

Scanning electron microscope (SEM) observations of SS–15Zr (e.g., [4,5]) show eutectic microstructures with approximately equal fractions of iron solid-solution and Fe–Cr–Ni–Zr materials. The iron solid-solution areas in an alloy of type 304 stainless steel and 15% Zr are ferrite [6]; alloys with type 316 stainless steel contain both ferrite and austenite [5]. The Fe–Cr–Ni–Zr materials are often referred to as 'intermetallics' or 'Laves phases' because of their similarities to Fe_2Zr and $Fe_{23}Zr_6$.

Chemical compositions of intermetallic areas in SS–15Zr have been interpreted as representing $Fe_{23}Zr_6$ and the C15 (cubic, $MgCu_2$-type) and C36 (dihexagonal, $MgNi_2$-type) polytypes of Fe_2Zr [6,7]. Materials with these structures are known to be present from neutron-diffraction data [5,6]. A material whose crystal structure is similar to that of the C14 (hexagonal, $MgZn_2$-type) polytype of Fe_2Zr occurs in SS–42Zr and may also be present in small quantities in SS–15Zr [5]. The Fe_2Zr polytypes cannot be distinguished from each other in SEM images [5,6]; $Fe_{23}Zr_6$ has a distinctive polygonal crystal habit (e.g., [6]).

The maximum observed actinide concentrations in three demonstration-scale metallic waste form ingots

* Tel.: +1-208 533 7478; fax: +1-208 533 7863.
E-mail address: dawn.janney@anlw.anl.gov (D.E. Janney).

0022-3115/$ - see front matter © 2003 Elsevier B.V. All rights reserved.
doi:10.1016/j.jnucmat.2003.08.032

from conditioning of EBR-II driver fuel (U–10wt%Zr) were 9 wt% for U, 10 ppm for Np, and 32 ppm for Pu, respectively [8]. These Np and Pu concentrations are too low for convenient detection by electron microscopy, and simulated metallic waste forms consisting of SS–15Zr with realistic concentrations of U and elevated concentrations of Np and Pu are commonly used in materials-characterization and corrosion studies (e.g., [8–11]).

SEM images of simulated metallic waste forms [8,12] show eutectic microstructures similar to those in SS–15Zr. The actinide elements are located almost entirely in the intermetallic phases [8]. Although actinide concentrations can vary markedly within a small area, there are no clear boundaries between adjacent high- and low-actinide areas. Neutron-diffraction data from SS–15Zr–5U show the presence of materials with the C15 Fe_2Zr, C36 Fe_2Zr, and $Fe_{23}Zr_6$ structures. Electron-diffraction data from SS–15Zr–5U–2Tc [8] confirm the presence of the C15 and C36 polytypes of Fe_2Zr and indicate that this sample also contains the C14 and six-layer hexagonal (6H) [13,14] Fe_2Zr polytypes.

Experimental measurements of elemental releases during immersion tests of actinide-bearing simulated metallic waste forms show that the normalized release rate of U is higher than that of any other element [10,11]. Previous attempts to understand this behavior have included characterization of actinide-bearing phases using SEM and neutron-diffraction data [8,9]. The SEM data provide information about the chemistry of actinide-bearing phases and suggest possible phase identifications to be used in interpreting diffraction data, but do not allow direct identification of crystal structures. Neutron-diffraction data can confirm phase identifications based on chemical data and provide information about crystal structures, but do not identify chemical compositions corresponding to each structure.

This report summarizes research involving characterization of host phases for actinides in simulated metallic waste form ingots with nominal compositions SS–15Zr–5U (referred to as '5U' in the rest of this paper), SS–15Zr–11U–0.6Rh–0.3Tc–0.1Pd ('11U'), SS–15Zr–2Np ('2Np'), and SS–15Zr–10Pu ('10Pu'), where numbers indicate weight percents of constituent elements and 'SS' indicates that the remaining material is Type 316 stainless steel. SEM [8,9], preliminary transmission electron microscope (TEM) [15,16], and neutron-diffraction [8,9] data from these ingots have been previously reported. The research has two goals: (1) perform chemical and structural characterization of significant host phases for actinide elements, with particular attention to relationships between structures and compositions, and (2) identify any other materials characteristics that might be relevant to understanding the high normalized release rate for U in dissolution experiments.

2. Experimental

Demonstration-scale ingots of 2Np, 5U, 11U, and 10Pu were prepared by melting metal charges in yttrium oxide crucibles, holding them at 1600 °C under flowing argon for 1–2 h, and cooling them to room temperature slowly (<10 °C/min). Each of these ingots weighs 10–30 g, as compared to 30–50 kg for production-scale ingots [8].

TEM samples of 2Np and 5U were prepared by cutting slices from the outer parts of the ingots with a low-speed saw, grinding the slices to a thickness of <100 μm, and breaking them into small pieces. Some of the pieces were individually ground to a maximum thickness of 30 μm, ending with a 1200-grit finish on each side. Each of these pieces was glued to a single-hole copper TEM grid and ion milled to perforation. Samples of 10Pu and 11U were prepared by cutting slices from the ingots, grinding to a thickness of ~200–300 μm, and producing 3 mm diameter disks with a disc punch. Each disk was individually ground to a thickness of ~50–90 μm, ending with a 1200-grit finish on one side. The side without the 1200-grit finish was dimpled with 0–2 μm cubic boron nitride abrasive to an estimated thickness of 20 μm at the bottom of the dimple and ion milled to perforation.

TEM observations were carried out using a JEOL 2010 TEM operating at 200 kV and equipped with a double-tilt (±20°, ±30°) analytical sample holder and an Oxford Link energy-dispersive X-ray spectroscopy (EDX) detector with a SiLi crystal and ISIS Suite Revision 3.2 software. Diffraction and EDX data were collected from a number of areas in each sample, allowing exact correlation of crystallographic and chemical characteristics in these areas. In some cases, it was possible to identify distinctive diffraction patterns diagnostic of particular crystal structures at the microscope. When this was not possible, the specimen was tilted through the entire range allowed by the specimen holder and all zone-axis diffraction patterns with closely spaced reflections were recorded for later measurement and identification. EDX spectra were also collected from areas without diffraction data to document chemical variability within single crystals and entire samples.

Crystal structures were identified by comparing d-spacings and interplanar angles from experimental selected-area electron diffraction patterns to those produced by candidate structure models from phases with similar compositions. When possible, lattice parameters from neutron-diffraction observations of SS–15Zr [5] were substituted for those from pure Fe–Zr phases while retaining the original space groups. Lattice parameters in 5U differ slightly from those in SS–15Zr [8]; however, these differences are too small to influence structure identifications. The structure models used were ferrite, austenite, C14 Fe_2Zr [5], C15 Fe_2Zr [17,18], C36 Fe_2Zr

[17,19], $Fe_{23}Zr_6$ [17,20], tetragonal [17,21] and cubic [17,22] polymorphs of $FeZr_2$, $FeZr_3$ [17,23], hexagonal and orthorhombic polymorphs of $FeZr_4$ [17,24], α-Zr [25], β-Zr [25], and ω-Zr [25]. Information about the six-layer structure observed in SS–15Zr–5U–2Tc [8] was not complete enough to allow calculations of interplanar spacings and angles; however, diffraction patterns from this phase would be readily recognizable because of the closely spaced reflections produced by the large stacking periodicity.

The C36 Fe_2Zr and $Fe_{23}Zr_6$ structures produce distinctive diffraction patterns when viewed from some crystallographic orientations, and thus in many cases can be identified at the microscope. When viewed from other orientations, both structures can also produce diffraction patterns similar to those representing major zone axes in the C15 Fe_2Zr structure. (The C14 Fe_2Zr structure can also produce single diffraction patterns similar to those representing the C15 structure. However, the C14 structure can generally be eliminated as a possible identification because it cannot produce all of the experimental diffraction patterns observed in a tilting survey from a single area.) Stereographic projections and simulated diffraction patterns demonstrate that the entire reciprocal space of both the C36 Fe_2Zr and $Fe_{23}Zr_6$ structures is within 20° of a zone axis with closely spaced reflections producing a distinctive diffraction pattern. As a consequence, at least one distinctive pattern can be observed when any sample with either of these structures is tilted through the full range allowed by the specimen holder. Thus, the absence of these patterns in tilting experiments is considered diagnostic of the C15 Fe_2Zr structure in areas where it can produce all of the individual experimental diffraction patterns.

Collection times for EDX data ranged from 50 to 1200 live seconds, depending on the importance assigned to finding and identifying small peaks. The ISIS software was used to quantify Fe, Cr, Ni, and Zr in 5U, 11U, and 2Np, U in and 5U and 11U, and Fe, Cr, and Ni in 10Pu. Quantification of Np in 2Np and of Pu and Zr in 10Pu required a different approach based on fundamental principles of spectrum generation and data reduction for EDX data collected in a TEM.

Quantification of intensities from EDX spectra collected in a TEM commonly uses proportionality constants called '*k*-factors' or 'Cliff-Lorimer factors' relating the relative intensities of X-rays from two elements to their relative masses (e.g., [26]). When relative masses of all elements of interest have been determined, they can be converted to absolute concentrations by appropriate normalization. Thus, the approximate concentration of Np relative to that of Fe (C_{Np}/C_{Fe}) in each spectrum from 2Np was calculated using the ratio of the intensities of the Np L_α and Fe K_α X-rays (I_{Np}/I_{Fe}) and the *k*-factor ($k_{Np/Fe}$) relating the two:

$$\frac{C_{Np}}{C_{Fe}} = k_{Np,Fe}\frac{I_{Np}}{I_{Fe}}. \quad (1)$$

Calculation of the approximate concentration of Pu relative to that of Fe given the relative intensities of X-rays from both elements is similar.

k-Factors relating relative intensities of Np and Pu X-rays to those of any other element were not available. However, fitting a cubic polynomial relating L_α *k*-factors supplied by the ISIS software to atomic numbers for Ce through Bi (atomic numbers 58–83) produced an excellent fit (*R*-value >0.999). *k*-factors for Np L_α and Pu L_α were approximated by extrapolating this polynomial to Np and Pu (atomic numbers 93 and 94).

X-ray intensities for Np were calculated for each spectrum from intermetallic materials in 2Np by interpolating a linear background across an energy window including the Np L_α peak and calculating the above-background intensity under the peak. A similar approach was used to calculate the intensity for the Zr K_α peak for comparison to that produced by the ISIS software. Although intensities for Zr K_α peaks calculated by subtraction of a linear background are significantly larger than those from ISIS, Zr concentrations calculated using both intensities agree to within a few percent. This difference is comparable to that between Zr contents calculated by the ISIS software using the Zr K_α and Zr L_α peaks.

EDX spectra collected from 10Pu with the electron beam turned off contain large peaks whose energies correspond to U and Np L-series characteristic X-rays and smaller peaks with energies corresponding to Cr K_α, Fe K_α, Fe K_β, Ni K_α, and Zr K_α X-rays. These spontaneously generated peaks result from phenomena other than interactions between the sample and the electron beam, and their intensities cannot be converted to chemical compositions representing specific areas of the sample in the usual manner. The U and Np peaks also appear in data spectra collected with the beam on. Intensities of the U and Np peaks relative to peaks corresponding to elements known to be present in data spectra can be reduced by increasing the count rate during spectrum collection. However, the U and Np peaks overlap (sometimes much smaller) Pu peaks that do not appear in the spontaneously generated X-ray spectrum. Thus, the U and Np peaks must be removed before the intensities of the Pu peaks can be calculated. This removal was done by subtracting the intensity in each channel of a spontaneously generated spectrum from the intensity in the corresponding channel of a data spectrum. Intensities for Zr and Pu X-rays were then determined by calculating the intensities above a linear background in a manner similar to that used in 2Np. Fig. 1 shows an example.

In EDX data from 10Pu, concentrations of Zr calculated by the ISIS software using Zr K_α and Zr L_α

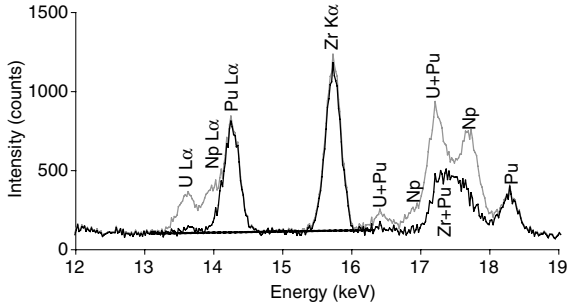

Fig. 1. An example of subtraction of a spontaneously generated X-ray spectrum and linear background from a data spectrum, sample 10Pu. Only intensities corresponding to energies between 10 and 20 keV are shown. Gray line: the data spectrum as collected. Black line: the data spectrum after channel-by-channel subtraction of a spontaneously generated X-ray spectrum collected with the beam off. Heavy line: the linear background model. Concentrations of Zr and Pu were calculated from the intensities in the Zr K_α and Pu L_α peaks after subtraction of the spontaneously generated spectrum and linear background.

X-rays without removal of spontaneously generated X-rays commonly differ by 10–20%; differences of 30% occur in a few spectra. In most cases, zirconium concentrations calculated from the intensity of the Zr K_α peak after subtraction of a spontaneously generated spectrum and a linear background fall between the values calculated by the ISIS software using the Zr K_α and Zr L_α peaks. The exceptions occur in spectra with very large numbers of counts, where all three measures of zirconium concentration agree to within a few percent.

In this paper, concentrations of Np and Pu are expressed as intensity ratios between the Np or Pu L_α and Zr K_α peaks and as elemental fractions. All compositions are normalized so that the total of the atomic fractions of Cr, Ni, Fe, Zr, and actinide elements is 1. This normalization ignores small concentrations of Mn, which the ISIS software indicated were present in some spectra but which could not be verified because of peak overlaps.

3. Results

The data in this section are based primarily on TEM examination of seven specimens: two of 5U, two of 11U, one of 2Np, and two of 10Pu. Several of the TEM samples were examined more than once, with additional ion milling to expose new areas of the specimen between examinations. Most of the samples had several ion-milled holes tens or hundreds of microns apart.

3.1. 5U

SEM data were collected by Dr. Tom O'Holleran from a slice of 5U before small amounts were extracted for preparation as TEM samples. Most of the sample has a eutectic microstructure typical of that reported from SS–15Zr samples (e.g., [4,5]). However, several areas with polygonal crystals at edges of cracks lined with a high-Zr material were observed (Fig. 2). X-ray mapping shows small high-Zr regions within the polygonal crystals. Small (<1 μm across) high-actinide areas separate some of the polygonal crystals. The morphology of the polygonal crystals [27–29] and their association with Zr [29] are characteristic of $Fe_{23}Zr_6$.

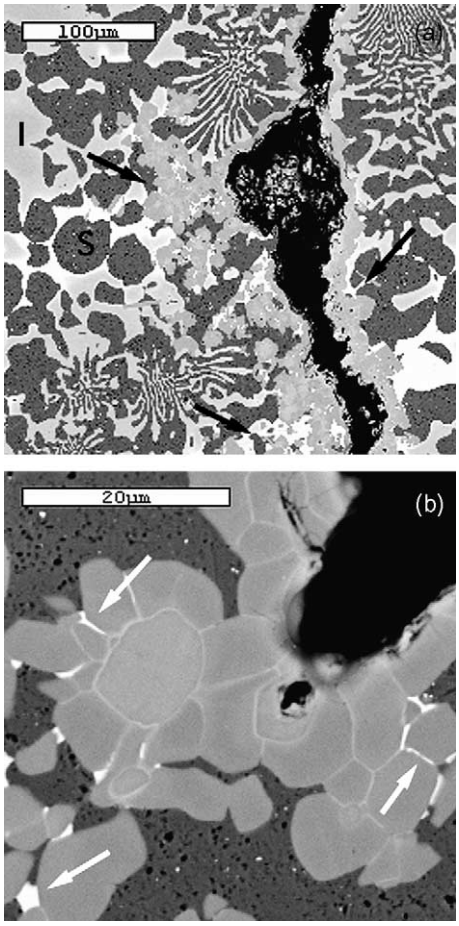

Fig. 2. SEM back-scattered electron images of 5U (courtesy of Dr. Tom O'Holleran). Medium-gray areas indicated by 'S' are steel; lighter areas indicated by 'I' are intermetallic. Within the intermetallic areas, the color indicates the actinide content: lighter areas have higher concentrations of U. (a) Zr-lined crack with associated areas of polygonal crystals, probably $Fe_{23}Zr_6$. The black area extending from the top to the bottom of the image is the crack itself. Arrows indicate examples of polygonal crystals. These features are unusual; most of the sample has eutectic microstructures similar to those at the edges of the figure. (b) Small white areas (examples at arrows) indicate high-actinide regions between polygonal crystals at the edge of a crack or hole in the specimen.

Table 1
Major-element composition ranges in intermetallic materials

Sample	Structure	Minimum and maximum elemental compositions, at.%. Estimated errors: ±5% for 5U, 11U, and 2Np; ±10% for 10Pu				
		Cr	Ni	Fe	Zr[a]	Actinide[b]
5U	C15 Fe_2Zr	5–7	14–21	52	13–26	1–9
	C36 Fe_2Zr	5–8	11–18	50–57	23–29	0–1
	$Fe_{23}Zr_6$	5–10	8–17	59–65	11–23	0–6
11U	C15 Fe_2Zr	3–7	12–20	51–57	8–22	2–17
	C36 Fe_2Zr	6–8	11–13	55–57	21–23	2–4
2Np	C15 Fe_2Zr	5–7	21–32	41–53	14–24	1–2 (0.05–0.15)
10Pu	C15 Fe_2Zr	4–11	13–23	42–50	9–29	4–17 (0.34–3.81)

[a] Calculated by the ISIS software for 5U, 11U, and 2Np, and by subtraction of spontaneously generated X-rays and a linear background for 10Pu.
[b] Numbers in parentheses are intensity ratios of Np or Pu L_α to Zr K_α X-rays.

TEM data from intermetallic phases in 5U include more than 75 zone-axis diffraction patterns and 45 EDX spectra. Most of the data are from areas with the C36 Fe_2Zr structure. However, several crystals with the $Fe_{23}Zr_6$ structure were found in a specimen prepared from an area where SEM data indicated that this phase was common, and a few areas with the C15 Fe_2Zr structure were also identified. Compositions from EDX data from intermetallics in 5U (Table 1) may show slight differences between the different crystal structures; however, the variation within each structure is at least as large as that between structures.

Many images from intermetallics in 5U show closely spaced planar defects, sometimes occurring in more than one crystallographic orientation within the same area (Fig. 3). The defects end at dislocations, some of which are at intersections with other defects. There are no detectable changes in crystallographic orientation, diffraction patterns, or chemical compositions associated with the defects. Thus, the defects are not twin boundaries, grain or subgrain boundaries, thin precipitates with compositions significantly different from those of the host crystal, or phase boundaries. All of the observed characteristics are consistent with the identification of the defects as stacking faults representing local offsets in the layered structure.

Two EDX spectra were collected from steels in 5U. Both show distinct Mo peaks, one has a small Ar peak, and neither has detectable U. Because the steel is clearly not a major U-bearing material in this sample, no attempt was made to determine whether it was ferritic or austenitic.

3.2. 11U

TEM data from intermetallic phases in 11U include more than 65 zone-axis diffraction patterns and 55 EDX spectra, representing over 20 areas. Three EDX traverses, each containing multiple spectra from different parts of the same crystal to explore intracrystalline chemical variability, were also collected.

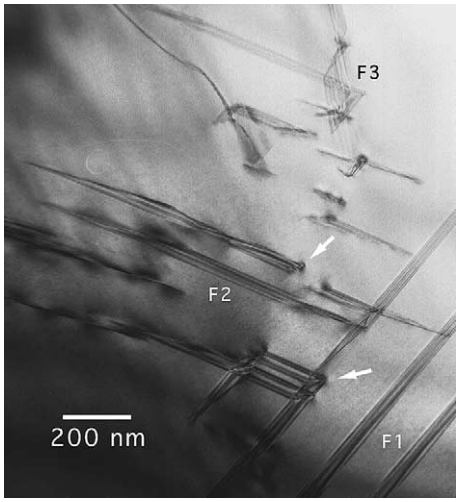

Fig. 3. Stacking faults in 5U (after [16]). F1, F2, and F3 indicate stacking faults with three orientations. Arrows show examples of dislocations at ends and intersections of stacking faults. Changes in contrast at dislocations indicate elastic strain.

Intermetallics with C15 Fe_2Zr and C36 Fe_2Zr structures were observed in 11U. Diffraction patterns from C36 Fe_2Zr from appropriate orientations show closely spaced reflections corresponding to interplanar spacings of 1.6 nm. Strong streaks through these reflections suggest a high-density of stacking faults along planes with this spacing (Fig. 4). Transitions between the C15 Fe_2Zr and C36 Fe_2Zr structures are sharp.

EDX spectra from material with the C36 Fe_2Zr structure are relatively homogeneous and contain at

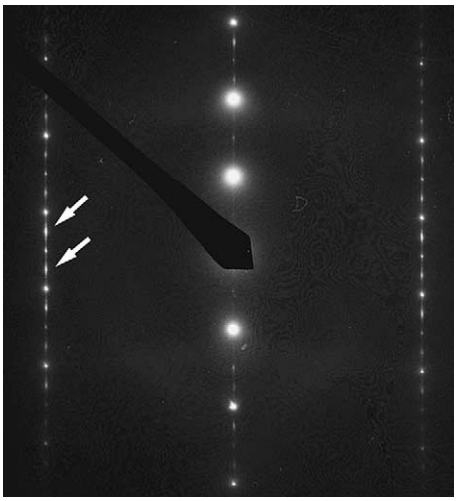

Fig. 4. Diffraction pattern from 11U shows closely spaced reflections from planes with 1.6 nm spacings representing the stacking periodicity of the C36 Fe_2Zr structure. Strong streaking (examples at arrows) indicates a high density of stacking faults along planes perpendicular to the closely spaced reflections.

most 5 at.% U (Table 1). In contrast, spectra from C15 Fe_2Zr display significant variation in major-element concentrations and U concentrations between 2 and 20 at.%. There is little difference in composition between C36 Fe_2Zr and adjacent areas of C15 Fe_2Zr.

Three EDX spectra were collected from steel in 11U. All show distinct Mo peaks, and most show small Tc peaks. One of the spectra has detectable U (as well as significant concentrations of Si, Ar, and other elements suggesting that material from outside the area being observed had been introduced during ion milling). The data indicate that steel is not a major U-bearing material in this sample, and no attempt was made to determine whether it was ferritic or austenitic.

3.3. 2Np

Data from intermetallic phases in 2Np include approximately 75 zone-axis diffraction patterns, representing 12 symmetrically non-equivalent zone axes, 20 areas, and at least seven crystals. (The number of crystals represented in the data depends on how twins are counted.) Approximately 40 EDX spectra were collected from these materials. All but one of the crystals was identified as having the C15 Fe_2Zr structure. The remaining crystal, which produced closely spaced reflections inconsistent with the C15 Fe_2Zr structure, was a grinding fragment embedded in epoxy in a bubble or crack in the original ingot. The diffraction data did not permit identification of this fragment because of the limited tilt range from which it was visible, and it is not considered further here.

All of the EDX data from intermetallic phases in 2Np show low Np concentrations (Table 1). A series of EDX spectra were collected at approximately equally spaced points in the electron-transparent area where the edge of an ion-milled hole crossed a single crystal. Spectra collected close to boundaries with adjacent crystals have relatively high-Ni/Fe ratios that are distinctly different from spectra collected farther from the edges of the crystal in the plane of the specimen (which may, however, have been close to the edges of the crystal in the third dimension). Differences between adjacent spectra suggest sharp compositional gradients without changes in crystal structure. The variation in compositions within this crystal is only slightly smaller than that observed in the entire sample.

Ferritic and austenitic steels were identified in 2Np. Both kinds of steel contain detectable Mo, and neither contains significant quantities of actinides.

3.4. 10Pu

Data from 10Pu include 75 zone-axis diffraction patterns representing approximately 40 areas. The data represent at least five materials: two Fe–Zr intermetallics with distinctly different concentrations of zirconium, small high-Pu inclusions in one of the intermetallics, a high-Pu material with significant Mo, and steel.

Most of the Fe–Zr intermetallic materials observed in 10Pu have 10–25 at.% Zr and the C15 Fe_2Zr structure (Table 1). Images show a characteristic mottled appearance indicating structural or compositional variation on a scale of a few nm or tens of nm. Twinning is common (Fig. 5), and planar defects ending at dislocations were observed.

The remaining data from 10Pu are from two distinct regions of the same TEM specimen. These regions included a number of crystals with Zr concentrations between 65 and 90 at.% and two crystals from a material with approximately 40 at.% Pu, 25–30% Fe, and 20% Mo. Small rounded inclusions with high Pu contents were observed at a subgrain boundary in the high-Zr materials. Strongly exposed diffraction patterns from the high-Mo material and most crystals of the adjacent high-Zr materials have several rings indicating the presence of a nanocrystalline material distinct from that in the single-crystal patterns.

The Fe–Zr phase diagram has a eutectic composition at ~91 at.% Fe, and stable phases in Fe–Zr alloys with bulk compositions >66 at.% Fe are α-Fe, Fe_2Zr, and $Fe_{23}Zr_6$ (e.g., [25,28,30]). Previous SEM and neutron-diffraction observations of SS–15Zr indicate that its composition represents a similar eutectic. Thus, the high-Zr crystals and adjacent materials probably represent an area of incomplete mixing when the sample ingot

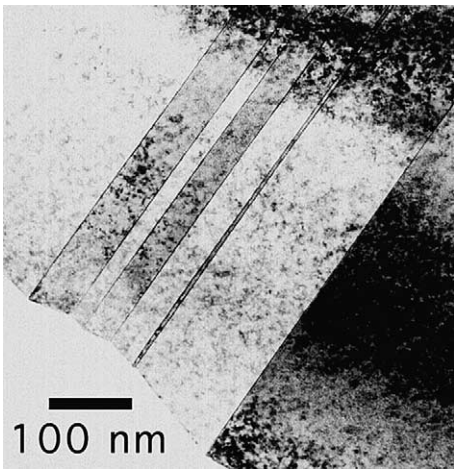

Fig. 5. Twinning in the C15 Fe_2Zr intermetallic structure, 10Pu. The mottled appearance is characteristic of this material. The offset grain boundary at the left ends of the twins accommodates shearing strain associated with formation of the twins.

was cast. Despite the high Pu contents of some of these materials, they are not believed to represent significant actinide-bearing phases in production-scale ingots.

Twelve EDX spectra and 13 diffraction patterns were collected from steel in nine areas of the 10Pu specimens. Three of these areas are ferritic; structures of the others were not determined. Much of the steel data was collected at the edges of holes with thick, irregular or lobate, edges, apparently occurring where the ion-milled surfaces intersected bubbles or cracks formed during casting of the ingot. Spectra from these areas show significant concentrations of Zr and Pu, probably reflecting inclusion of characteristic X-rays from the immediately adjacent thick areas. Spectra from well-thinned areas show small Pu and Zr peaks representing concentrations of at most a few atomic percent, but otherwise closely resemble EDX spectra from steel in the other specimens. Thus, steel is apparently not a significant Pu-bearing material.

4. Discussion

4.1. Comparison to previous results

Neutron powder-diffraction studies of the 5U ingot reported that it contained 13% C36 Fe_2Zr, 21% C15 Fe_2Zr, and 17% $Fe_{23}Zr_6$ [8,9]. These identifications are consistent with those reported here. However, proportions of the various crystal structures observed in this study differ significantly from those in the neutron-diffraction study, as well as between the two 5U samples studied here.

In comparing chemical compositions measured in this study to those reported previously, it is convenient to present compositions graphically. Figs. 6–9 compare compositions reported by Keiser et al. [8] to EDX spectra from this study. Elements are listed along the X-axis, with Cr and Ni adjacent to emphasize possible differences in Cr/Ni ratios. Atomic fractions are along the Y-axis, normalized to $Cr + Ni + Fe + Zr + actinides = 1$. Each line connects atomic fractions for a single chemical composition.

Comparison of Figs. 6 and 7, which show data from 5U and 11U respectively, shows that the 'other Laves' compositions reported by Keiser et al. [8] are consistent with data from the C15 and C36 Fe_2Zr structures in this study. Data from materials with the $Fe_{23}Zr_6$ structure in this study are limited but suggest that material with the low U concentration of the 'other Laves' materials may also have lower Ni concentrations than any of the materials reported by Keiser et al. [8]. The 'U-rich Laves' composition in 11U [8] is similar to the highest-U spectrum from the C15 Fe_2Zr structure in this study and has a significantly higher concentration of U than was observed in any other structure. These comparisons suggest that areas of 'U-rich Laves' in both 5U and 11U have the C15 Fe_2Zr structure; the 'other Laves' areas in these specimens could be either C36 Fe_2Zr or C15 Fe_2Zr.

Fig. 8 compares compositions observed in this study to those reported by Keiser et al. [8] from 2Np. Low-Ni spectra from materials with the C15 Fe_2Zr structure represent compositions similar to those of the 'other Laves' materials reported by Keiser et al. All actinide concentrations observed in this study are significantly below those in the 'actinide-rich Laves' of Keiser et al. [9]. Keiser et al. note that the fraction of high-actinide intermetallics increases with increasing actinide concentrations in the bulk composition of the sample; thus, the 'actinide-rich Laves' in 2Np may be a rare material. Its structure remains unknown.

Low-Ni spectra from materials with the C15 Fe_2Zr structure in 10Pu represent compositions similar to those of the 'other Laves' materials observed by Keiser et al. [8] (Fig. 9). The highest-Pu concentration in an area with diffraction data indicating the C15 Fe_2Zr structure is similar to that of the 'actinide-rich Laves' observed by Keiser et al.; however, Ni concentrations in the two materials are significantly different.

Neutron-diffraction observations of $Fe_{23}Zr_6$ in 5U suggest that the effects of U are larger than would be expected from the low (1.7 at.%) concentration observed in previous EDX analyses of 11U [8]. The present study may explain this discrepancy: although $Fe_{23}Zr_6$ crystals with U concentrations comparable to those reported by Keiser et al. [8] were observed in back-scattered SEM images and some of the EDX spectra collected with the TEM, others have significantly higher concentrations of U.

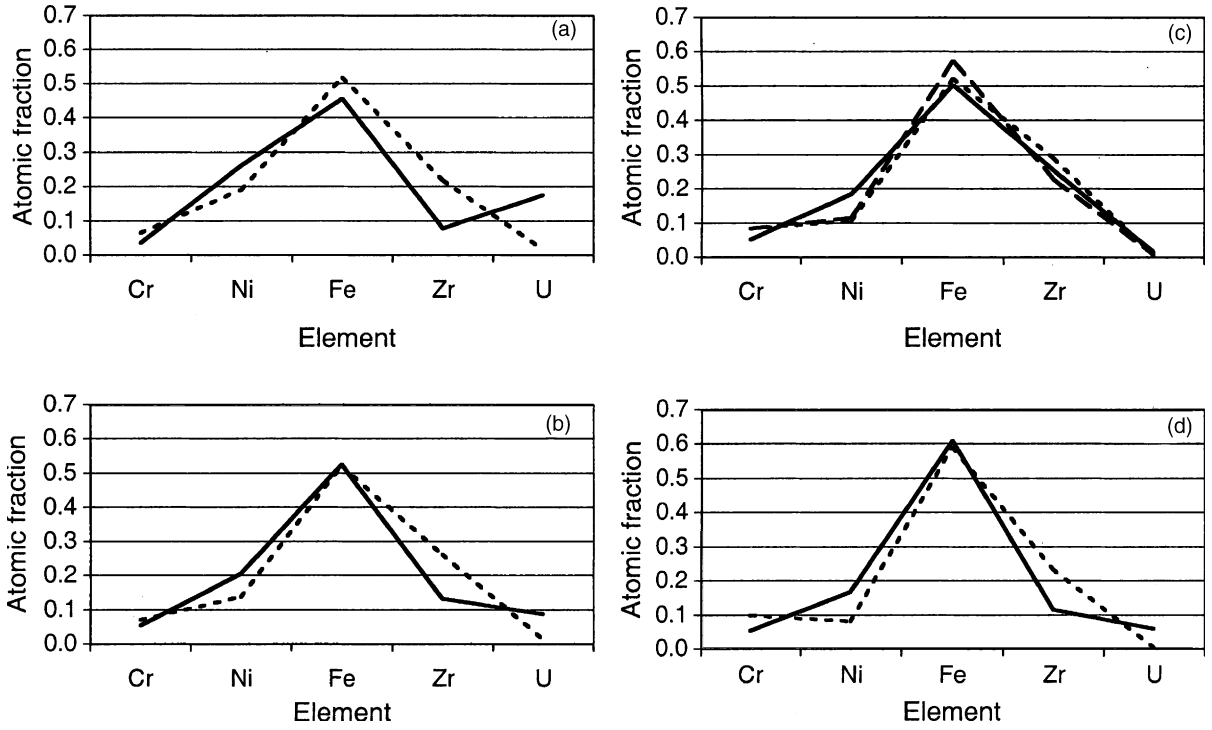

Fig. 6. Compositional variation in 5U. Elements are listed along the X-axis, with Cr and Ni adjacent to assist in evaluating the Cr/Ni ratio. Atomic fractions are along the *Y*-axis, normalized so that atomic fractions of Cr, Fe, Ni, Zr, and U total 1. Each line connects atomic fractions for a single composition. Solid and dashed lines in (a) indicate sources of data. Spectra in (b)–(d) represent analyses with the highest and lowest fractions of each element shown; solid and dashed lines emphasize similarities and differences between these spectra and those in (a). (a) 'U-rich Laves' (solid line) and 'other Laves' (dashed line) of Keiser et al. [8]. (b) Variation in the C15 Fe_2Zr structure. (c) Variation in the C36 Fe_2Zr structure (after [16]). (d) Variation in the $Fe_{23}Zr_6$ structure.

Most of the differences between the results of Keiser et al. [8,9] and those reported here are likely consequences of the small sample volumes and number of crystals represented in the TEM data in all three papers and the spatially inhomogeneous distribution of phases in the samples (e.g., Fig. 2).

It has been stated that the main compositional difference between C15 and C36 Fe_2Zr phases in alloys of type 316 stainless steel with 15 wt% Zr is the Ni/Cr ratio, which is >2.5 for C15 Fe_2Zr, ~1.5 for C36 Fe_2Zr, and ~1 for $Fe_{23}Zr_6$ [6]. EDX analyses from a TEM study of SS–15Zr–5U–2Tc [8] were consistent with these results. Results from this study confirm that the highest Ni/Cr ratios in the C36 Fe_2Zr and $Fe_{23}Zr_6$ structures are at the low end of the range for C15 Fe_2Zr. The lowest Ni/Cr ratio observed is from the $Fe_{23}Zr_6$ structure. Although all materials with high Ni/Cr ratios observed in the present study have the C15 Fe_2Zr structure, there are apparently no sharp distinctions between the Ni/Cr ratios of different structures.

Keiser et al. [8,9] noted that the sum of atomic percentages of U and Zr is essentially the same (~24%) in both high- and low-U Fe_2Zr intermetallics. The sum of Pu and Zr is also approximately 24%; that of Np and Zr is 21% in high-actinide areas and 14% in low-actinide ones. The data in Table 1 generally confirm these observations but suggest that the sum of Np and Zr in low-Np areas may be somewhat higher than previously reported. Keiser et al. suggested that the inverse relationship between U and Zr concentrations might represent substitution of U into Zr sites in the Fe_2Zr structure [8,9] and noted the existence of Fe_2U as a factor in favor of this explanation [8]. The structure of α-Fe_2Pu [31] is identical to those of C15 Fe_2Zr and Fe_2U [32], suggesting that substitution of Pu into Zr sites may explain the observed relationship between Pu and Zr concentrations in Pu-bearing Fe–Zr intermetallics.

The data presented here suggest significant compositional variability in intermetallic phases with the C15 Fe_2Zr structure in actinide-bearing SS–15Zr alloys. This variability is difficult to confirm from previous research in which compositions have been reported as single numbers (e.g., [4,5,33]). However, Fe–Zr phase diagrams show concentrations of Zr varying between ~27 and 34 at.% in C15 Fe_2Zr [28,30,34]. (Compositional variability in C36 Fe_2Zr is less well understood, although variation

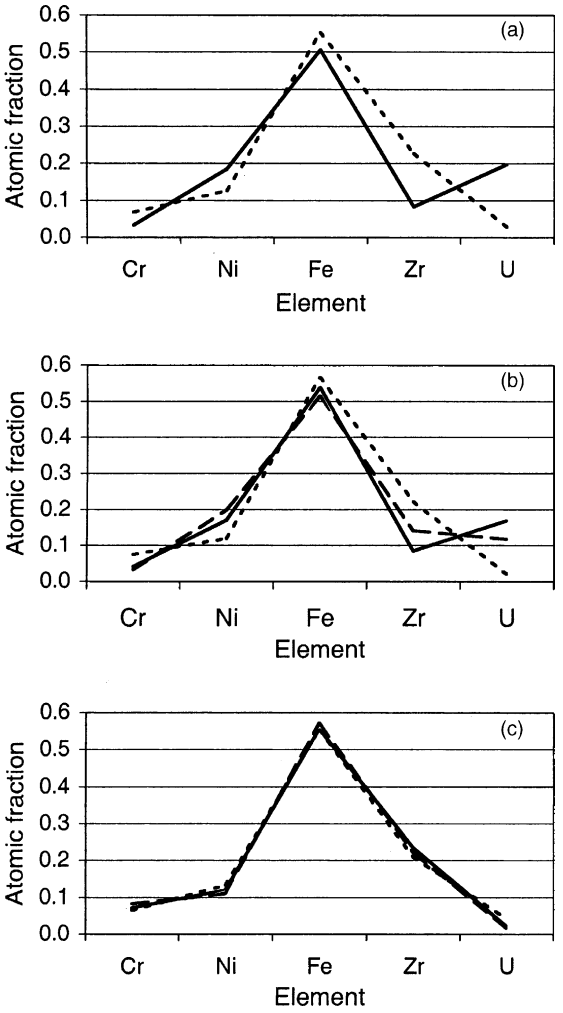

Fig. 7. Compositional variation in 11U, plotted as in Fig. 6. (a) 'U-rich Laves' (solid line) and 'other Laves' (dashed line) of Keiser et al. [8]. (b) Variation in the C15 Fe_2Zr structure (after [16]). (c) Variation in the C36 Fe_2Zr structure (after [16]).

between 27.3 and 31.4 at.% Zr has been observed [19], and $Fe_{23}Zr_6$ has a fixed composition [4,5,33].) The compositional variability shown by the data in this paper suggests possible extensive substitution between atoms of different elements in the C15 Fe_2Zr structure. The evidence for substitution of actinides in Zr sites has been summarized above. Brückner et al. [35] performed a detailed analysis of site occupancies in a sample of C15 Fe_2Zr with 27.7 at.% Zr and concluded that some Zr sites are occupied by Fe. References to Fe_2Zr-type intermetallics in SS–15Zr as $Zr(Fe,Cr,Ni)_{2+x}$ (e.g., [4,5,33]) may imply substitution of Cr and Ni into Fe sites. However, any discussions of site occupancies and substitutions in actinide-bearing SS–15Zr should be regarded as speculative until detailed structural analyses are performed.

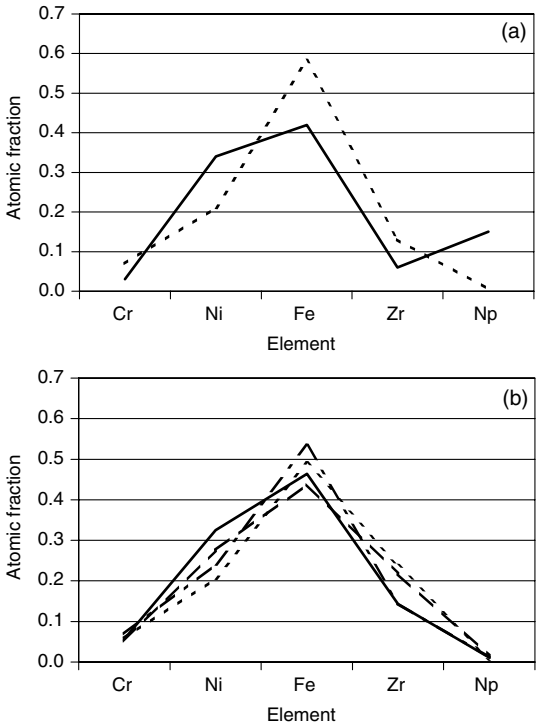

Fig. 8. Compositional variation in 2Np, plotted as in Fig. 6. (a) 'Actinide-rich Laves' (solid line) and 'other Laves' (dashed line) of Keiser et al. [8]. (b) Variation in the C15 Fe_2Zr structure (after [16]).

Keiser et al. [8,9] suggested that U concentration gradients in SS–15Zr–5U–2Tc might reflect the presence of a series of related Fe_2Zr polytypes, each with a different actinide concentration, and that the highest concentration of U should occur in the C15 Fe_2Zr structure because of its cubic character. The observed U concentrations in 5U and 11U confirm that U concentrations in the C15 Fe_2Zr structure are generally higher than those in the C36 Fe_2Zr structure, and a boundary separating regions of these two structures might appear as an actinide concentration gradient in SEM images. However, the data from 11U do not support the idea that compositional gradients reflect a series of polytypes if the concentration of U is more than 5 at.% (the apparent upper limit for U in the C36 Fe_2Zr structure). Instead, all of the observed actinide concentrations can occur in the C15 Fe_2Zr structure, which can be both a 'U-rich' and 'other' Laves phase in the sense of Keiser et al. [8]. Thus, it is likely that all of the high-actinide areas and some of the low-actinide ones in SEM images of 5U and 11U, and probably also of 10Pu, have the C15 Fe_2Zr structure, and the observed smooth transitions between high- and low-actinide areas represent chemical gradients in this structure.

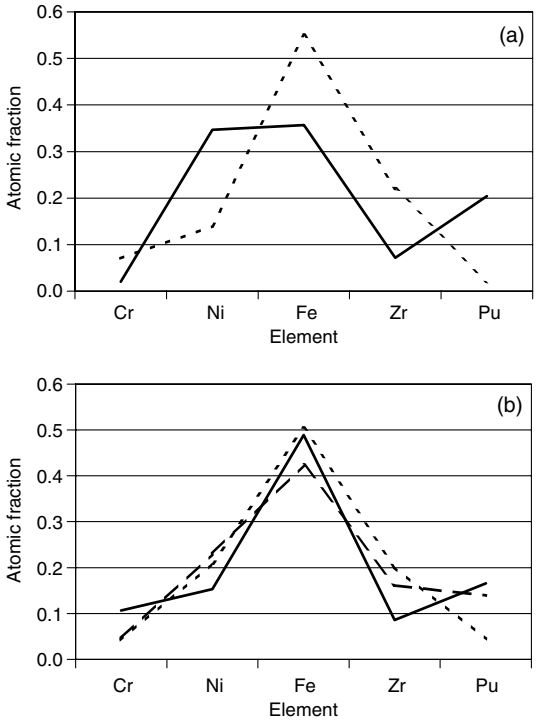

Fig. 9. Compositional variation in 10Pu, plotted as in Fig. 6. (a) 'Actinide-rich Laves' (solid line) and 'other Laves' (dashed line) of Keiser et al. [8]. (b) Variation in the C15 Fe_2Zr structure (after [16]).

4.2. Microstructures

The structures of the Fe_2Zr polytypes are commonly described by analogy to close-packed structures of atoms of a single element, although the actual packing units in Fe_2Zr are structurally complex [14]. The $MgZn_2$ (C14) structure is hexagonal and has a two-layer (ABAB) stacking sequence. The $MgCu_2$ (C15) structure is cubic, with a three-layer (ABCABC) sequence. The $MgNi_2$ (C36) structure has a four-layer (ABACABAC) sequence [13,36,37]. Shear transformations involving migration of Shockley-type partial dislocations in these structures can produce phase transitions and mechanical twinning [14,38].

Stacking faults were commonly observed in both U-bearing samples, but rarely seen in 10Pu and 2Np. Stacking faults and coherent twin planes are both low-energy defects relative to grain boundaries; however, the energy of a stacking fault is generally about twice that of a twin plane in a close-packed material [39]. Etching experiments exploiting increased dissolution rates at intersections between dislocations and material surfaces have been used to investigate deformation microstructures in a variety of materials (e.g., [40,41]). A rigorous argument about the relationship between defects and dissolution rate requires information about stacking-fault and dislocation energies that is not currently available. However, it seems plausible that the stacking faults and associated dislocations may increase the dissolution rate of both U samples.

The stacking faults and twinning in the C15 Fe_2Zr structure are similar to those produced by deforming a Fe–10at.%Zr alloy by a compressive strain of ~47% at room temperature [38]. Microhardness measurements of SS–15Zr made with a 1000-g load and 10-s loading time averaged 380 HK (~370 HV), and produced fine cracks in the intermetallic materials [5]. Although quantitative determinations of stacking-fault and dislocation densities were not attempted, dislocation densities in steels in some areas of the dimpled samples (11U and 10Pu) appeared generally lower than those in 5U and 2Np, which were prepared by gluing thin fragments to grids. Stacking faults appeared somewhat less commonly in 11U than in 5U, particularly in crystals near steels with relatively low dislocation densities. These observations suggest that deformation microstructures may have been introduced into the intermetallic materials during TEM sample preparation. More extensive introduction of deformation microstructures may have occurred while finishing the surfaces of U-bearing samples for immersion tests with an abrasive wheel on a Dremel tool [11]. Other possible reasons why U-bearing samples tend to have more stacking faults than those with Pu or Np include orientation of the specific crystals examined relative to the applied stress responsible for the deformation and differences in stacking-fault energies and dislocation mobility between U-bearing intermetallic materials and those with other actinides.

The present data indicate that the major U- and Pu-bearing phase has the C15 Fe_2Zr structure. Thus, differences in dissolution behavior between U and Pu must be caused by something other than different crystal structures of the high-actinide phases. A defect-related increase in the dissolution rate of the U-bearing materials may be part of the answer, but requires either a dissolution mechanism favoring the release of U or preferential retention of other elements in corrosion products to explain the dissolution-experiment results of Johnson et al. [10,11]. Other possible structural and microstructural factors influencing dissolution behavior may include a composition-dependent dissolution rate for C15 Fe_2Zr or differences in volume fractions and dissolution rates for the C15 and C36 Fe_2Zr structures in the different samples.

5. Conclusions

Relationships between crystal structures and compositions of actinide-bearing materials were studied in

samples from four ingots using TEM. The TEM data include approximately 300 single-crystal diffraction patterns and 250 EDX analyses. A small amount of new SEM data was also collected. The nominal sample compositions are SS–15Zr–2Np ('2Np'), SS–15Zr–5U ('5U'), SS–15Zr–11U–0.6Rh–0.3Tc–0.1Pd ('11U'), and SS–15Zr–10Pu ('10Pu'). Previous SEM and neutron-diffraction studies of other parts of these ingots were reported by Keiser et al. [8].

Iron solid solutions ('steels') and material with the C15 Fe_2Zr (cubic, $MgCu_2$-type) structure were observed in all four samples. The C36 Fe_2Zr structure was found in 5U and 11U, and the $Fe_{23}Zr_6$ structure was observed in 5U. Several other materials were identified in an area of incomplete mixing in the 10Pu ingot.

Relationships between structures, compositions, and microstructures in these materials can be summarized as follows:

1. Phase identifications in 5U are consistent with those reported from neutron-diffraction data [8]. Relative frequencies with which the phases were observed in the present data differ significantly from the previously reported volume fractions. These discrepancies are likely consequences of the small sample volume and number of crystals represented in the TEM data and the spatially inhomogeneous distribution of the phases. For similar reasons, it is likely that the actual compositional variation in each phase exceeds that represented in the present data.
2. Materials with the C15 Fe_2Zr structure are compositionally variable. Observed actinide concentrations range from 1 to 15 at.% for U and Pu. All observations of material with the C15 Fe_2Zr structure in 2Np have approximately 1% Np.
3. Materials with the $Fe_{23}Zr_6$ structure in 5U are also compositionally variable. The data represent only a few crystals but indicate U concentrations ranging from 0 to at least 5 at.%. This variation may explain why previous neutron-diffraction data [8] indicated that addition of U affected lattice parameters in $Fe_{23}Zr_6$ more than would be expected from previous SEM data indicating a U content of 1.7 at.%.
4. Materials with the C36 Fe_2Zr structure in 5U and 11U have limited compositional variability and contain at most 5 at.% U.
5. Steels are not significant actinide-bearing materials in any sample.
6. The present data generally agree with previous research [8] showing that the Ni/Cr ratio is highest in the C15 Fe_2Zr structure and lowest in $Fe_{23}Zr_6$. However, the lowest-Ni analyses from the C15 Fe_2Zr structure are similar to the highest-Ni analyses from the C36 Fe_2Zr and $Fe_{23}Zr_6$ structures, and there are no sharp distinctions in the Ni/Cr ratios from the three structures.
7. The distinction between 'actinide-rich Laves' (including 'U-rich Laves') and 'other Laves' materials in the SEM data of Keiser et al. [8] does not correspond to a clear difference in crystal structures. Low-actinide areas with the C15 Fe_2Zr structure have compositions similar to those reported for 'other Laves' materials in all samples; these compositions are similar to some of those observed in the C36 Fe_2Zr and $Fe_{23}Zr_6$ structures in 5U and 11U. Thus, 'other Laves' materials may have the C15 Fe_2Zr, C36 Fe_2Zr, or $Fe_{23}Zr_6$ structure. The 'actinide-rich Laves' material in 5U, 11U, and 10Pu probably has the C15 Fe_2Zr structure. Actinide-content gradients observed in SEM images probably represent compositional variations within the C15 Fe_2Zr structure.
8. The observed inverse correlation between concentrations of Pu and Zr is similar to the previously reported correlation between U and Zr concentrations [8], which is confirmed in this study. These correlations may be explained by substitution of actinide elements into Zr sites.
9. Stacking faults and associated dislocations were commonly observed in the 5U and 11U samples but rarely seen in 10Pu and 2Np. They may contribute to an increased dissolution rate for intermetallics in U-bearing samples. However, this possible increase does not by itself explain the observed differences between elemental proportions in the sample and those in the solution.

Acknowledgements

Argonne National Laboratory is operated for the US Department of Energy by the University of Chicago. This work was supported by the US Department of Energy, Office of Nuclear Energy, Science, and Technology, under contract W-31-109-ENG-38. I thank Dr Tom O'Holleran for providing the new SEM data on 5U (including Fig. 2), Dr Jan-Fong Jue for assistance with sample preparation, and Dr Wharton Sinkler for providing indexing and diffraction-pattern-simulation software. Drs Dennis Keiser, Steve Johnson, and Jan-Fong Jue graciously discussed their unpublished data. I also thank Ms Tanya Barber, Mr Mark Surchik, Mr Tom DiSanto, and Ms Marianne Noy.

References

[1] P. Ackerman, T.R. Johnson, L.S.H. Chow, E.L. Carls, W.H. Hannum, J.J. Laidler, Prog. Nucl. Energy 31 (1997) 141.
[2] S.M. McDeavitt, D.P. Abraham, J.Y. Park, D.D. Keiser Jr, JOM 49 (1997) 29.
[3] R.W. Benedict, S.G. Johnson, D.D. Keiser, Jr., T.P. O'Holleran, K.M. Goff, S.M. McDeavitt, W. Ebert, in:

Plutonium Futures–The Science, Santa Fe, NM, 10–13 July 2000.
[4] D.P. Abraham, S.M. McDeavitt, J.Y. Park, Metall. Mater. Trans. A 27A (1996) 2151.
[5] D.P. Abraham, J.W. Richardson Jr, S.M. McDeavitt, Mater. Sci. Eng. A 239&240 (1997) 658.
[6] D.P. Abraham, J.W. Richardson Jr, in: G.E. Fuchs, K.A. Dannemann, T.C. Deragon (Eds.), Long Term Stability of High Temperature Materials, TMS, Warrendale, PA, 1999, p. 169.
[7] D.P. Abraham, N. Dietz, Mater. Sci. Eng. A 329 (2002) 610.
[8] D.D. Keiser Jr, D.P. Abraham, W. Sinkler, J.W. Richardson Jr, S.M. McDeavitt, J. Nucl. Mater. 279 (2000) 234.
[9] D.D. Keiser Jr, W. Sinkler, D.P. Abraham, J.W. Richardson Jr, S.M. McDeavitt, in: R.G. Bautista, B. Mishra (Eds.), Rare Earths and Actinides: Science, Technology and Applications IV, TMS, Warrendale, PA, 2000, p. 111.
[10] S.G. Johnson, M. Noy, T. DiSanto, T.L. Barber, in: B.P. McGrail, G.A. Cragnolino (Eds.), Scientific Basis for Nuclear Waste Management XXV, Materials Research Society Symposium Proceedings, vol. 713, Materials Research Society, Warrendale, PA, 2002, p. 705.
[11] S.G. Johnson, M. Noy, T. DiSanto, S.M. Frank, D.D. Keiser Jr, Radioact. Waste Mange. Environ. Restorat. 22 (2002) 300.
[12] D.D. Keiser Jr, D.P. Abraham, J.W. Richardson Jr, J. Nucl. Mater. 277 (2000) 333.
[13] X.Y. Meng, D.O. Northwood, J. Less Common Met. 125 (1986) 33.
[14] C.W. Allen, K.C. Liao, Phys. Status Solidi A 74 (1982) 673.
[15] D.E. Janney, Microsc. Microanal. 8 (supplement 2) (2002).
[16] D.E. Janney, in: R.J. Finch, D.B. Bullen (Eds.), Scientific Basis for Nuclear Waste Management XXVI, Materials Research Society Symposium Proceedings, vol. 757, Materials Research Society, Warrendale, PA, 2003, p. 343.
[17] P. Villars, L.D. Calvert, Pearson's Handbook of Crystallographic Data for Intermetallic Phases, vol. 3, ASM International, Materials Park, OH, 1991.
[18] V.N. Svechnikov, V.M. Pan, A.T. Spektor, Russ. J. Inorg. Chem. 8 (1963) 1106.
[19] K. Kai, T. Nakamichi, M. Yamamoto, J. Phys. Soc. Jpn. 25 (1968) 1192.
[20] P.I. Kripyakevich, V.S. Protasov, E.E. Cherkashin, Russ. J. Inorg. Chem. 10 (1965) 151.
[21] E.E. Havinga, H. Damsma, P. Hokkeling, J. Less Common Met. 27 (1972) 169.
[22] Y.B. Kuz'ma, V.Y. Markiv, Y.V. Voroshilov, R.V. Skolozdra, Inorg. Mater. 2 (1966) 222.
[23] F. Aubertin, U. Gonser, S.J. Campbell, H.-G. Wagner, Zeit. Metallkd. 76 (1985) 237.
[24] K.H.J. Buschow, J. Less Common Met. 79 (1981) 243.
[25] T.B. Massalski (Ed.), Binary Alloy Phase Diagrams, 2nd Ed. and updates, ASM International, Materials Park, OH, 1990.
[26] J.I. Goldstein, D.B. Williams, G. Cliff, in: D.C. Joy, A.D. Romig Jr, J.I. Goldstein (Eds.), Principles of Analytical Electron Microscopy, Plenum, New York, 1986, p. 155.
[27] Y. Liu, S.M. Allen, J.D. Livingson, Scr. Metall. Mater. 32 (1995) 1129.
[28] C. Servant, C. Gueneau, I. Ansara, J. Alloys Compd. 220 (1995) 19.
[29] D.P. Abraham, J.W. Richardson Jr, S.M. McDeavitt, Scr. Mater. 37 (1997) 239.
[30] M.S. Granovsky, D. Arias, J. Nucl. Mater. 229 (1996) 29.
[31] H. Okamoto, in: M.E. Kassner, D.E. Peterson (Eds.), Phase Diagrams of Binary Actinide Alloys, ASM International, Materials Park, OH, 1995, p. 314.
[32] H. Okamoto, in: M.E. Kassner, D.E. Peterson (Eds.), Phase Diagrams of Binary Actinide Alloys, ASM International, Materials Park, OH, 1995, p. 164.
[33] S.M. McDeavitt, D.P. Abraham, J.Y. Park, J. Nucl. Mater. 257 (1998) 21.
[34] D. Arias, M.S. Granovsky, J.P. Abriata, in: H. Okamoto (Ed.), Phase Diagrams of Binary Iron Alloys, ASM International, Materials Park, OH, 1993, p. 467.
[35] W. Brückner, K. Kleinstück, G.E.R. Schulze, Phys. Status Solidi 23 (1967) 475.
[36] M. O'Keeffe, B.G. Hyde, Crystal Structures I. Patterns and Symmetry, Mineralogical Society of America, Washington, DC, 1996.
[37] C.S. Barrett, T.B. Massalski, Structure of Metals, 3rd Ed., McGraw-Hill, New York, 1966.
[38] Y. Liu, J.D. Livingson, S.M. Allen, Metall. Trans. A 23A (1992) 3303.
[39] J.P. Hirth, J. Lothe, Theory of Dislocations, 2nd Ed., Krieger Publishing Company, Malabar, FL (USA), 1992.
[40] R.E. Reed-Hill, Physical Metallurgy Principles, 2nd Ed., PWS-KENT Publishing Company, Boston, MA, 1973.
[41] R.E. Smallman, Modern Physical Metallurgy, 4th Ed., Butterworths, London, 1985.